International Journal of GEOMATE, April, 2025 Vol.28, Issue 128, pp.125-132
ISSN: 2186-2982 (P), 2186-2990 (O), Japan, DOI: https://doi.org/10.21660/2025.128.g14307
Geotechnique, Construction Materials and Environment

OPTIMAL GEOGRID WEIGHT AND FAILURE MODES OF GEOGRID ENCASED STONE COLUMNS UNDER AXIAL COMPRESSION LOADING WITH COST CONSIDERATIONS

Wittawat Yodsomjai[1], Chana Phutthananon[2], *Pornkasem Jongpradist[3], Suraparb Keawsawasvong[4], and Pitthaya Jamsawang[5]

[1,2,3]Department of Civil Engineering, Faculty of Engineering, King Mongkut's University of Technology Thonburi, Thailand, [4]Department of Civil Engineering, Thammasat School of Engineering, Thammasat University, Thailand, [5]Soil Engineering Research Center, Department of Civil Engineering, King Mongkut's University of Technology North Bangkok, Thailand

*Corresponding Author, Received: 16 Nov. 2024, Revised: 05 Feb. 2025, Accepted: 07 Feb. 2025

ABSTRACT: This study investigates the efficiency of geogrid encasement in stone columns under axial compression loading, with a focus on cost-effectiveness and performance. A three-dimensional finite element analysis is conducted using PLAXIS 3D to evaluate the ultimate bearing capacity, lateral displacement behavior, and failure mechanisms of encased stone columns (ESCs). The load-settlement response and lateral displacement profile along the column depth are analyzed to determine the optimal geogrid encasement configuration. The results indicate that, for a fixed geogrid weight, a thinner but longer encasement significantly enhances the ultimate bearing capacity and minimizes lateral displacement compared to a thicker but shorter encasement. Furthermore, three primary failure mechanisms under axial compression loading are identified: column head failure, column body-soil interaction failure, and soil failure, with the governing failure mode dependent on column geometry and encasement parameters. Based on these findings, the study proposes an optimal geogrid weight guideline for ESC applications, offering a balance between material efficiency and performance. Additionally, a design chart is developed to illustrate the relationship between ultimate bearing capacity and geogrid weight, providing engineers with a systematic approach for preliminary ESC design. These insights contribute to advancing cost-effective and high-performance geotechnical solutions using ESCs, optimizing their application in ground improvement projects.

Keywords: Bearing capacity, Failure, Stone column, Geogrid, Numerical analysis

1. INTRODUCTION

The ordinary stone columns (OSCs) are a widely-used soil stabilization technique for reinforcing soft subsoil foundations. OSCs are often used to support embankments, liquid storage tanks, warehouses, raft foundations, and low-rise structures [1–3]. This soil stabilization technique can improve the properties of soft soil and address associated issues by enhancing both bearing capacity and drainage capabilities. Additionally, this technique can significantly reduce the settlement of the stabilized subsoil foundations [4, 5]. Typically, the bearing capacity of OSCs comes from the circumferential confinement stress provided by the surrounding soils. However, in extremely soft soils with an undrained shear strength of less than 15 kPa, where circumferential confinement stress from the surrounding soil is insufficient, OSCs may not provide adequate bearing capacity and could exhibit excessive radial deformations [6, 7].

To address the aforementioned issues, the concept of increasing circumferential confinement stress by encasing OCSs with high-stiffness, creep-resistant geosynthetic materials was introduced by Van Impe [8]. This type of composite stone column is known as an encased stone column (ESC). The encasement effectively provides additional circumferential confinement to the OSC by mobilizing tensile forces in the geosynthetics, thereby reducing the lateral stress and strain developed in both the column and the surrounding soils under axial compression loading [9]. Consequently, the geosynthetic encasement is the most critical component influencing the performance of ESCs. The axial stiffness and encasement length of the geosynthetic material are two key factors in the design of ECSs, directly impacting both performance and cost. Numerous researchers (e.g., [10–13]) have investigated the effect of geosynthetic axial stiffness on the load-carrying behavior of ESCs. Their findings suggest that using geosynthetics with high axial stiffness increases the vertical stress on the column while reducing the lateral stresses transmitted to the surrounding soils. This characteristic reduces the reliance of the bearing capacity of ESCs on the strength of the surrounding soil while also mitigating both lateral bulging and settlement. However, previous studies observed that bulging occurred at a greater depth and resulted in a smaller extent of bulging failure compared to that observed in OSCs. It should be noted that the geosynthetic encasement length may need to be extended in cases where the ground is weaker [14, 15]. Importantly, employing

geosynthetic encasement with excessive tensile stiffness and length does not always guarantee an increase in bearing capacity or a reduction in settlement. Instead, it primarily serves to prevent bulging deformations of the column [16]. Therefore, the cost-effectiveness of ESCs depends significantly on selecting geosynthetic materials that achieve an optimal balance between axial stiffness and encasement length [17].

As extensively reviewed, several previous studies have focused solely on the cost-effectiveness of ESCs using controlled geogrid with equal encasement length or axial stiffness to determine the optimum encasement length and axial stiffness. These studies have not yet investigated the performance of ESCs based on equivalent geogrid costs by controlling the weight of geogrid. Since the cost of geogrid is correlated with the quantity of geogrid material used to encase OSCs, which is determined by its weight per unit area, this study investigates the performance of ESCs in terms of ultimate bearing capacity, lateral displacement, and failure patterns using the three-dimensional (3D) finite element method with PLAXIS 3D. Besides, equivalent geogrid encasement weights along the column are also considered to introduce the concept of optimizing encasement to achieve the highest performance efficiency under controlled costs.

This paper begins by outlining the research significance in Section 2 and describing the finite element (FE) modeling for the proposed study in Section 3. Section 4 presents the preliminary FE investigation results, followed by Section 5, which discusses the parametric analysis and provides guidelines for selecting appropriate geogrid weights. Finally, Section 6 summarizes the key findings of this study.

2. RESEARCH SIGNIFICANCE

The study introduced an approach to examine the effects of stiffness and length of geogrid encasement on the performance of single ECS under axial loading, with an emphasis on cost-effectiveness; an aspect not addressed in previous research. This objective can be achieved by controlling the weight of the geogrid, allowing for variations in axial stiffness and encasement length while maintaining equivalent costs, thus providing an appropriate framework for the design of ECSs. 3D FE analyses were employed to simulate the behavior of ECSs under axial loading, offering valuable insights into their performance in terms of bearing capacity, lateral bulging, and failure behavior. These analyses ultimately contribute to the development of optimal guidelines for geogrid encasement. The findings provide essential insights for the design and implementation of ECSs in similar projects, focusing on cost-effective solutions.

3. DETAILS OF THE REFERENCE CASE AND FINITE ELEMENT MODELING

3D FE simulations were performed to gain a better understand of the efficiency of geogrid encasement in both ESCs and OSC. First, the adopted FE modeling procedure was validated by comparing the computed results with data from a history case of field ESC column load test, as reported by Yoo and Lee [14] in terms of the axial load-settlement curve at the head of ESCs and horizontal displacement along their depth. Then, the validated FE modeling was used to further examine the ultimate bearing capacity, lateral displacement, and failure pattern of ECSs (investigated cases for this study), assuming their installation within the soft Bangkok clay located in the lower central region of Thailand. In this study, the subsoil profile and parameters was adopted from the previous work of Phutthananon et al. [18]. This subsoil profile was chosen to examine the performance of ESCs and OSC due to the well-documented material parameters. Additionally, the subsoil profile is more uniform compared to the case history.

3.1 Geological Condition of Reference Case

The subsoil profile of the reference case consists of a 6.6 m-thick layer of Bangkok soft clay, followed by a 3.4 m-thick layer of medium stiff clay. Beneath this layer, a 15 m-thick layer of stiff clay is present. The groundwater table is situated approximately 1.5 m below the ground surface. ESCs with a diameter of 0.5 m and a length of 5.6 m were designated as the reference column case. In all investigated cases, the top of the column is positioned 1.0 m below the ground surface, with the column tip resting on the medium stiff clay layer. The configurations of the reference column case and subsoil profile were successfully used to investigate both conventional and geogrid-encased deep cement mixing columns, as reported in previous studies [18, 19].

3.2 FE Modeling

3.2.1 FE Mesh and Boundary Condition

A series of 3D FE simulations were carried out to simulate column load tests using the commercial software PLAXIS 3D. Figure 1 illustrates an example of the generated FE mesh used for the analysis. The FE model, with dimensions of 10 m in both the x- and y-directions and 25 m in the z-direction, contained approximately 37,000 elements. The column and soils were modeled using 10-node tetrahedral elements, while 6-node triangular plate elements were used to model both the geogrid and the rigid steel plate. The rigid steel plate was placed on top of the column to facilitate uniform pressure distribution. To accurately simulate the soil-structure interaction

between the column and the surrounding soils, interface elements were included with an appropriate value for the strength reduction factor (R_{inter}). At the lateral boundaries, soil movement was restricted horizontally but allowed vertically. Soil movement at the bottom surface was fixed in all directions, while at the top, soil movement was unrestricted in all directions. In the FE model, an impermeable boundary was assigned along the bottom and the four side boundaries. A zero pore-pressure boundary condition was set at the ground surface to allow free drainage.

3.2.2 Constitutive Model and Model Parameters

The hardening soil (HS) constitutive model was selected to simulate the behavior of both cohesive soils and stone columns in this study. The HS model is successfully used to simulate behavior of Bangkok subsoils [20, 21]. In this study, the HS parameters for cohesive soils were taken from the previous study by Phutthananon et al. [18], while the parameters for the stone column were adopted from Imam et al. [22]. The undrained condition was used to simulate the behavior of cohesive soils, while a drained condition was applied to the stone column. All required input parameters used for the HS model are listed in Table 1. A linear elastic (LE) model was used for the rigid steel plate and geogrid. The LE parameters for the rigid steel plate were set with a Young's modulus (E) of 10^{12} kPa and a Poisson's ratio of zero. The linear property of the biaxial geogrid was derived from its axial stiffness (EA), which varied from 750 to 3000 kN/m in this study (see Table 2 for details) [23]. A R_{inter} value of 1.0 was chosen to simulate the interaction between soil, column, and geogrid, given the sufficient interlocking between them [4, 24–28].

3.2.3 FE Analysis Procedure

To simulate the column load test, the FE analysis procedure was divided into five steps: (i) establishing the initial distributions of both vertical and horizontal soil stresses (using the unit weight of soil and the coefficient of earth pressure at rest) along with the initial pore water distribution in the form of a hydrostatic profile, (ii) excavating a 1-m-deep pit from the soil surface, (iii) installing the columns using the wish-in-place approach, (iv) positioning the rigid steel plate on top of the column, matching the column diameter, and (v) incrementally applying an axial load of 10 kN to the rigid steel plate until column failure was achieved. In this study, the ultimate bearing capacity (Q_{ult}) of the column was determined as the applied load corresponding to a column head settlement of 100 mm or approximately 20% strain relative to the column diameter, in this study column diameter is 0.5 m, based on the computed load-settlement curve [29]. Additionally, it is essential to verify that the tensile stress developed on the geogrid does not surpass its ultimate tensile strength to prevent any potential failure of the geogrid.

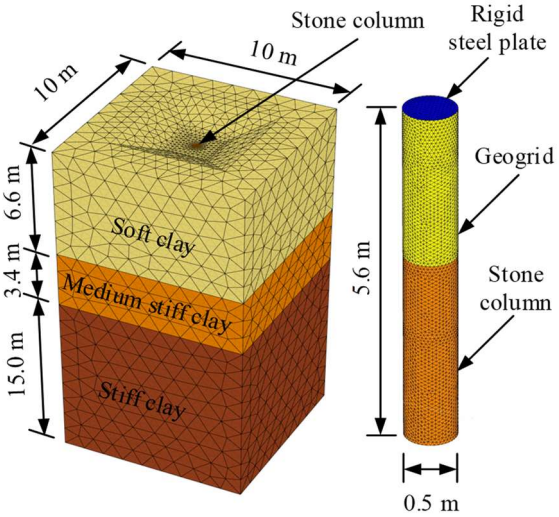

Fig. 1 Geometry and FE mesh employed in this study

Table 1. HS parameters used in FE analysis

Parameters	Soft clay	Medium stiff clay	Stiff clay	Stone column
E_{50}^{ref} (kPa)	5000	20000	60000	45000
E_{oed}^{ref} (kPa)	5000	20000	60000	45000
E_{ur}^{ref} (kPa)	15000	60000	180000	135000
ϑ_{ur} (–)	0.2	0.2	0.2	0.2
m (–)	1	1	1	0.3
K_0^{NC} (–)	0.625	0.625	0.625	0.293
γ (kN/m^3)	15	15	18	23
c' (kPa)	6	10	18	5
$\emptyset'$ (degree)	0	0	0	45
φ (degree)	0	0	0	10
R_f (–)	0.9	0.9	0.9	1.0
OCR (–)	1.1	2.0	2.5	1.0
p^{ref} (kPa)	100	65	95	100

Table 2. Properties of geogrid used in FE analysis

Axial stiffness, EA (kN/m)	Ultimate tensile strength, T_{ult} (kN/m)	Mass per unit area, W/A (g/m^2)
750	30	320
1500	60	620
3000	120	830

3.3. Verification of FE Modeling

A full-scale column load test conducted on the ESC was used to verify the FE modeling procedure of this study. The test site was located at Gimhae city, in

the southern region of South Korea. The test was conducted on ESC with a diameter of 0.8 m and a length of 5.4 m. The encasement length (L_e) and axial stiffness (EA) of the biaxial geogrid were 2.4 m and 2500 kN/m, respectively. The subsoil profile of this case history comprises a 0.7 m-thick layer of fill material underlain by a 1.8 m-thick layer of clayey sand. Below the clayey sand is a 1.1 m-thick layer of silty clay, followed by a 2.6 m-thick layer of gravelly sand overlying a layer of decomposed granite soil. The groundwater table was approximately 0.7 m below the ground surface. The subsoil profile and geometry of the FE model used for verification, are displayed in Figure 2. The HS parameters for the stone column and soils required for this verification are listed in Tables 1 and 3 [22], respectively.

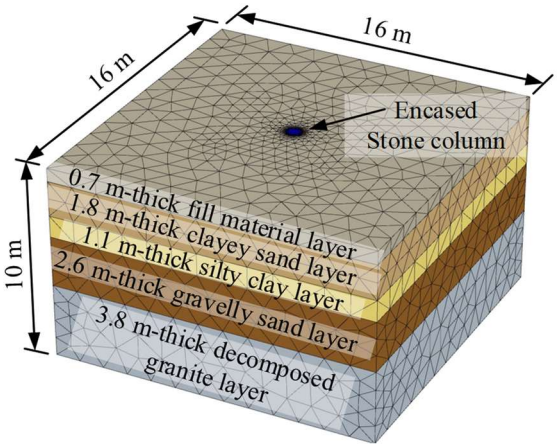

Fig. 2 Geometry and FE mesh employed in the verification of FE modeling

Table 3. HS parameters used in verification of FE modeling

Parameters	Fill	Clayey sand	Silty clay	Gravelly sand	Granite
E_{50}^{ref} (kPa)	12000	15000	850	25000	45000
E_{oed}^{ref} (kPa)	12000	15000	850	25000	45000
E_{ur}^{ref} (kPa)	36000	45000	2550	75000	135000
ϑ_{ur} (–)	0.2	0.2	0.2	0.2	0.2
m (–)	0.5	0.5	1.0	0.5	0.5
K_0^{NC} (–)	0.577	0.531	1.0	0.426	0.357
γ (kN/m^3)	18	19	20	20	21
c' (kPa)	4	4	24	2	2
$\emptyset'$ (degree)	25	28	-	35	40
φ (degree)	5	5	-	5	5
R_f (–)	1.0	1.0	1.0	1.0	1.0
OCR (–)	1.0	1.0	1.0	1.0	1.0
p^{ref} (kPa)	100	100	100	100	100

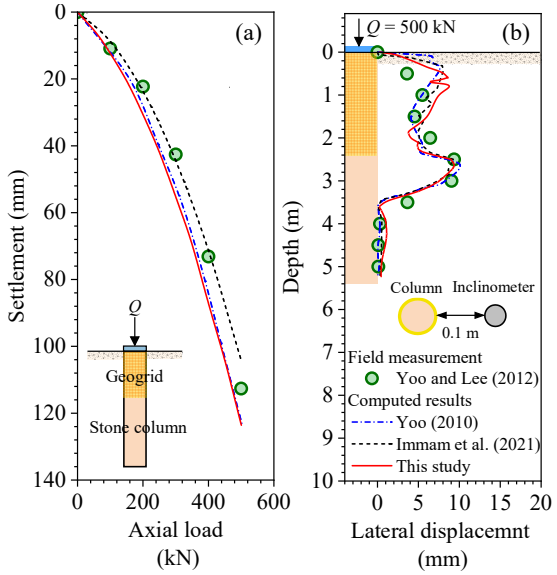

Fig. 3 Comparisons of field measurement data and computed results (a) axial load-settlement curves (b) lateral displacement along depth at an applied load 500 kN

Figures 3a and 3b show the comparison between the computed and measured results of axial load-settlement curves and lateral displacements along the depth of the ESC, respectively. In these figures, the computed results reported by Imam et al. [22] and Yoo [30] are also included. Upon inspection, it can be observed that the current FE model can be used to capture well the general trend of the measurement data, as well as the numerical results obtained from previous studies. Therefore, it can be confirmed that the FE modeling procedure used in this study is satisfactory and can be used with high confidence for further investigations.

4. PRELIMINARY INVESTIGATION

To comprehensively investigate the performance of geogrid encasement in terms of cost on Q_{ult}, lateral displacement along the depth, and failure pattern of ESCs, this study considered geogrid costs based on the quantity of geogrid material used to encase OSC. Therefore, the weight of the geogrid was used as a key parameter to gain insight into the performance of ESCs under comparable costs, which can be calculated using the following equation:

$$W_g = \pi D L_e (W/A) \quad (1)$$

where W_g is the weight of geogrid (g), D represents the column diameter (m), L_e represents the geogrid encasement length (m), and W/A refers to the mass per unit area of the geogrid (g/m^2).

Figure 4 presents the computed axial load-settlement curves of ESCs with different EA and L_e conditions under equivalent W_g values of 653.45 g

and 1960.35 g. For cases with W_g = 653.45 g, it can be observed that ESCs with a thinner but longer encasement length (i.e., EA = 750 kN/m and L_e = 1.30 m or EA750-L_e1.30) improve Q_{ult} more effectively than ESCs with a thicker but shorter encasement length (i.e., EA1500-L_e0.67 and EA3000-L_e0.50). In cases of ESCs with the same W_g of 1960.35 g, the optimum encasement scheme remains thinner but longer encasement length pattern. However, the enhancement Q_{ult} is less pronounced at EA = 750 kN/m (EA750-L_e3.90) compared to the lower geogrid weight condition. At this higher W_g, the optimum axial stiffness changes from EA = 750 kN/m to 1500 kN/m, because exceeding the optimum geogrid weight reduces the Q_{ult} gain rate. Further discussion of the optimum weight of geogrid is described in Section 5.

Figure 5 shows the lateral displacement along the depth for various geogrid encasements at an applied load of Q_{ult}. In this study, both the OSC and ESC are the end-bearing types. Thus, when the considered OSC and ESCs are subjected to loads at the top of the column, failure occurs in the form of lateral bulging in all cases. For OSC, maximum lateral bulging was observed at the upper section of the column near the ground surface. In contrast, for ESCs, maximum bulging typically occurred beneath the geogrid encasement, with some exception cases (e.g., EA750-L_e3.90, as shown in Fig 5b). Furthermore, it can be seen that when the columns are subjected to loads at the top, circumferential stress occurs within the column. In OSC, these stresses are concentrated in the upper section of the column, where the surrounding soil often provides inadequate lateral confinement. This situation can lead to lateral bulging of the column. However, encasing OSCs with geogrid can significantly mitigate this lateral bulging. This mechanism allows the geogrid to not only resist bulging displacement but also to transfer load from the stone particles into the geogrid, directing it downward to a deeper level. In sections of the column beneath geogrid encasement, the load is transmitted directly to the surrounding soil, leading to localized bulging. However, as depth increases, lateral confinement from the surrounding soil rises due to the overburden pressure, providing resistance against bulging. Consequently, this combined action results in less bulging deformation in ESCs compared to OSC.

In cases with a controlled weight of the geogrid of W_g = 653.45 and 1960.35 g, as depicted in Figs. 5a and 5b, respectively, it can be observed that ESCs with a thinner but longer encasement (i.e., EA750-L_e1.30 for W_g = 653.45 g or EA750-L_e3.90 for W_g = 1960.35 g) reduce lateral bulging more than ESCswith a thicker but shorter encasement

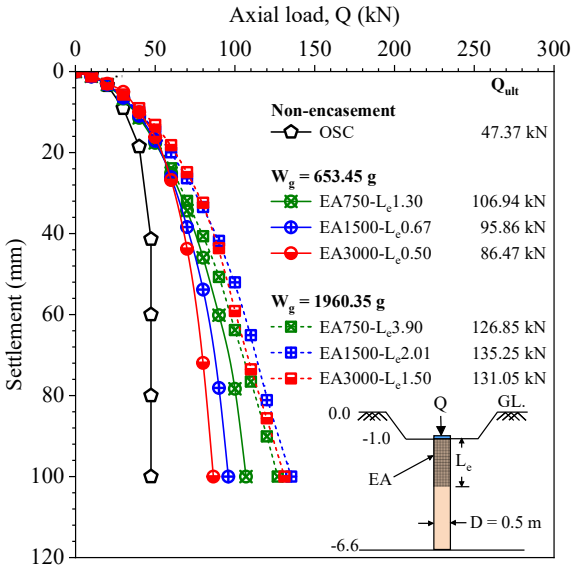

Fig. 4 Computed axial load-settlement curves with various geogrid encasements

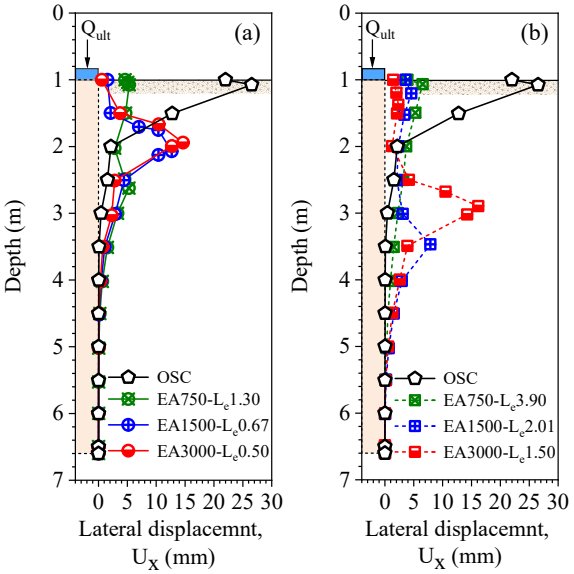

Fig. 5 Lateral displacement along the depth at applied failure load of OSC and ESCs with various geogrid encasements (a) W_g = 653.45 g and (b) W_g = 1960.35 g

(i.e., EA3000-L_e0.50 for W_g = 653.45 g or EA3000-L_e1.50 for W_g = 1960.35 g).

To examine the change in failure patterns of columns, the occurrence of plastic points, referred to as Mohr-Coulomb points (MCPs) in PLAXIS 3D, was monitored for the FE results at the applied load of Q_{ult}. Figure 6a presents the MCPs for OSC at the applied load of Q_{ult}, where a large number of MCPs are concentrated in the upper portion of the columns. Thus, the column head failure is the primary failure pattern of OSC. Figures 6b-e illustrate the MCPs

distributions for ESCs with different EA and L_e conditions. For all ESCs, it can be observed that geogrid encasement of OSCs significantly reduces MCPs at the top part of the column and shifts them to the deeper levels within the column body, with some portions of the stresses being transferred to the surrounding soil. However, beneath the geogrid encasement, the column body's capacity to resist these transmitted stresses is lower than in the section of the column top encased by the geogrid. This can lead to structural failure in the zone below the geogrid encasement.

For MCPs distributions in ESCs under a controlled W_g of 653.45 g, the failure pattern appears consistent, with the MCPs were found at the column head and beneath geogrid encasement (see Figs 6b-d). However, the occurrence of MCPs in ESCs with thinner but longer geogrid lengths (i.e. EA750-L_e1.30 see Fig. 6b) extends to deeper levels compared to cases with a thicker but shorter encasement length (i.e., EA1500-L_e0.67 and EA3000-L_e0.50 as seen in Figs. 6c and 6d, respectively). When the weight of the geogrid increases beyond the optimum value (i.e., EA750-L_e3.90), most MCPs appear in surrounding soil around the periphery of the geogrid encasement, particularly in the upper portion of the column, as shown in Fig. 6e. Additionally, a few MCPs can be observed beneath the geogrid encasement.

5. PARAMETRIC STUDY AND GUIDELINES FOR APPROPRIATE GEOGRID WEIGHT

In this section, the simulated results from the sensitivity study of OSC and ESCs under axial loading, obtained by varying the W_g through changes in L_e and EA, are presented and discussed in terms of Q_{ult}. A total of 32 numerical cases were analyzed. Figure 7 shows the relationship between the W_g and Q_{ult} for various analysis cases. The three main data sets in the figure represent three different EA values with each data set including results from cases with various W_g values under a controlled EA. For the data set with an EA of 750 kN/m, the Q_{ult} increases approximately nonlinearly with increasing W_g, from 47.37 kN at the beginning (W_g = 0, non-encased) to a maximum value of 131.17 kN at a W_g of 1960.35 g (equivalent to L_e = 3.90 m or approximately 8D). When W_g exceeds 1960.35 g, Q_{ult} remains unchanged, indicating that the optimum W_g for ESCs with an EA of 750 kN/m is 1960.35 g.

For ESCs with EA of 1500 and 3000 kN/m, the Q_{ult} also increases nonlinearly with increasing W_g, similar to the previous case. However, the final values of Q_{ult} for these two cases are higher than in the previous case, and the optimum W_g are 3911.29 g (equivalent to L_e = 4.02 m or approximately 8D) for an EA of 1500 kN/m and 5866.92 g (equivalent to L_e = 4.50 m or approximately 9D) for an EA of 3000 kN/m. When the W_g exceeds the optimum value, the failure mode of ESCs may change from column body-soil failure to soil failure. Further investigation of the failure behavior of ESCs with the optimum value of W_g revealed that the MCPs do not propagate into the column body beneath the geogrid encasement but instead extend into the surrounding soil at the top of the column up to failure, thereby changing the failure mode to soil failure, as displayed in Fig. 6e. As the W_g increases (which is equivalent to increasing L_e), soil failure consistently governs the behavior of the ESCs under axial compression loading, explaining the constant Q_{ult} with increasing W_g beyond the optimum value.

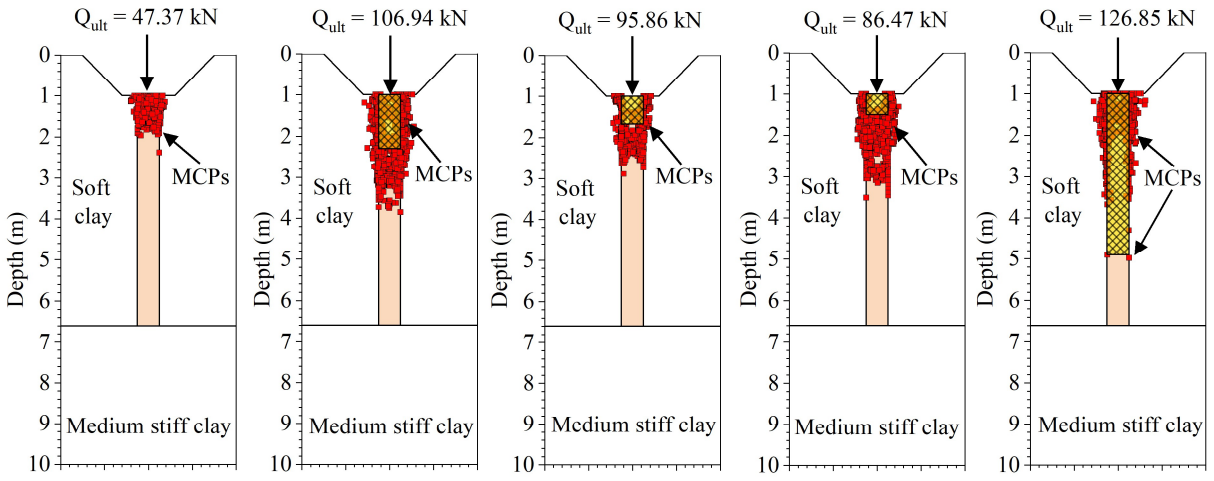

Fig. 6 Mohr-Coulomb points of ordinary stone column (OSC) and encased stone columns (ESCs) at failure load

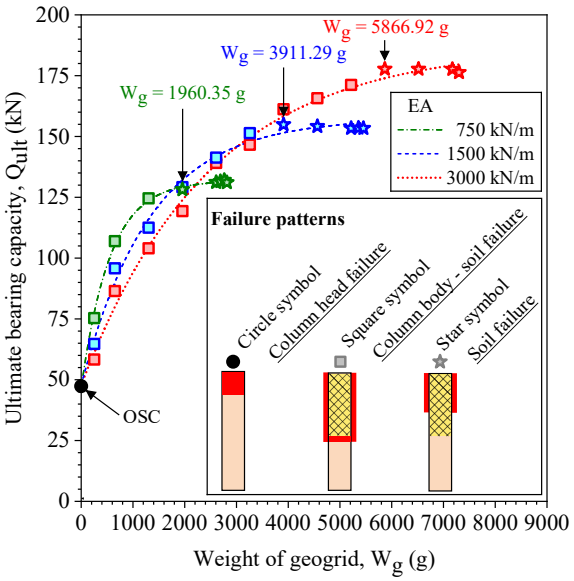

Fig. 7 Schematic diagram showing the relationship between W_g and Q_{ult} of OSC and ESCs with respect to failure modes

6. CONCLUSION

In this study, the performance of the ESCs under axial compression loading was investigated. A 3D-FE analysis was performed to examine the axial load-settlement response, ultimate bearing capacity, lateral displacement, and failure patterns of ESCs. The following conclusion can be drawn, based on the numerical results presented in this paper:

(1) Under controlled geogrid weight, using a thinner but longer geogrid encasement improves the ultimate bearing capacity and reduces lateral displacement of ESCs more effectively than using a thicker but shorter geogrid encasement. However, exceeding the optimal geogrid weight value diminishes the improvement in ultimate bearing capacity.

(2) The optimum geogrid weight for achieving better performance in terms of ultimate bearing capacity and preferable failure modes of ESCs, under cost consideration, depends on the stiffness, encasement length, and mass per unit area of geogrid.

(3) The three possible failure modes for OSC and ESCs under axial compression loading include column head failure, column body-soil failure, and soil failure. Column head failure occurs only in the case of OSC. Under controlled geogrid weight, the column body-soil failure mode occurs if the geogrid weight is lower than the optimum value. If the weight of the geogrid exceeds the optimum value, the failure mode changes to soil failure.

The optimum geogrid weight for the ESCs proposed in this study provides a guideline for the preliminary design of ESCs. The ultimate bearing capacity and geogrid weight chart offer a systematic approach for selecting an appropriate geogrid weight for preliminary design. However, further investigations using physical model tests or full-scale field tests are recommended to enhance the reliability of the conclusion in this study.

7. ACKNOWLEDGMENTS

The first author would like to express their gratitude for financial support from King Mongkut's University of Technology Thonburi (KMUTT) through The Petchra Pra Jom Klao Ph.D. scholarship under contract Grant No. 1/2565. The authors gratefully acknowledge the financial support provided by King Mongkut's University of Technology Thonburi (KMUTT), Thailand Science Research and Innovation (TSRI), and National Science, Research and Innovation Fund (NSRF) Fiscal year 2025 under the project titled "Innovation and advanced technology for future construction with sustainability", Grant number (FRB680074/0164). This research budget was allocated by the National Science, Research, and Innovation Fund (NSRF) and King Mongkut's University of Technology North Bangkok (Project no. KMUTNB-FF-68-A-05).

8. REFERENCES

[1] Dheerendra M.R., Nayak S. and Shivashankar R., A critical review of construction, analysis and behaviour of stone columns. Geotechnical and Geological Engineering, Vol. 31, Issue 1, 2013, pp. 1–22.

[2] Zhan Y., Jiang G. and Yao H., Dynamic characteristics of saturated silty soil ground treated by stone column composite foundation. Advances in Materials Science and Engineering, Vol. 2014, Issue 1, 2014, pp. 745386.

[3] Shirazi M.R., Zarrin O. and Valipourian K., The role of vibro-stone column for enhancing the soft soil properties. International Journal of Civil and Environmental Engineering, Vol. 9, Issue 5, 2015, pp. 616–620.

[4] Keykhosropur L., Soroush A. and Imam R., 3D Numerical analyses of geosynthetic encased stone columns. Geotextiles and Geomembranes, Vol. 35, 2012, pp. 61–68.

[5] Castro J., Karstunen M. and Sivasithamparam N., Influence of stone column installation on settlement reduction. Computers and Geotechnics, Vol. 59, 2014, pp. 87–97.

[6] Kadhim S.T., Parsons R.L. and Han J., Three-dimensional numerical analysis of individual geotextile-encased sand columns with surrounding loose sand. Geotextiles and Geomembranes, Vol. 46, Issue 6, 2018, pp. 836–847.

[7] Zhang L., Xu Z. and Zhou S., Vertical cyclic loading response of geosynthetic-encased stone column in soft clay. Geotextiles and

Geomembranes, Vol. 48, Issue 6, 2020, pp. 897–911.
[8] Impe Van W.F., Soil improvement techniques and their evolution. A.A. Balkema, Netherlands, 1989, pp. 1–131.
[9] Xu Z., Zhang L. and Zhou S., Influence of encasement length and geosynthetic stiffness on the performance of stone column: 3d dem-fdm coupled numerical investigation. Computers and Geotechnics, Vol. 132, 2021, pp. 103993.
[10] Fattah M.Y. and Majeed Q.G., A study on the behaviour of geogrid encased capped stone columns by the finite element method. International Journal of GEOMATE, Vol. 3, Issue 5, 2012, pp. 343–350.
[11] Hasan M., Ali I. and Hyodo M., Strength of soft clay reinforced with 10 mm single crushed coconut shell (ccs) column. International Journal of GEOMATE, Vol. 17, Issue 63, 2019, pp. 353-359.
[12] Vu M. N. and Dang Q. H., Analysis of stress transfer and distribution of an embankment on unreinforced and stone column-reinforced soft soils. International Journal of GEOMATE, Vol. 26, Issue 117, 2024, pp. 19-26.
[13] Baqir H. H., Aswad M. F. and Fattah M. Y., A numerical study on the behavior of stone columns with different area ratios in soft clays. International Journal of GEOMATE, Vol. 26, Issue 117, 2024, pp. 42-51.
[14] Yoo C. and Lee D., Performance of geogrid-encased stone columns in soft ground: full-scale load tests. Geosynthetics International, Vol. 19, Issue 6, 2012, pp. 480–490.
[15] Murugesan S. and Rajagopal K., Model tests on geosynthetic-encased stone columns. Geosynthetics International, Vol. 14, Issue 6, 2007, pp. 346–354.
[16] Mohamed M.K., Sakr M.A. and Azzam W.R., Geotechnical behavior of encased stone columns in soft clay soil. Innovative Infrastructure Solutions, Vol. 8, Issue 2, 2023, pp. 1–14.
[17] Ouyang F., Wu Z., Wang Y., Wang Z., Cao J., Wang K. and Zhang J., Field tests on partially geotextile encased stone column-supported embankment over silty clay. Geotextiles and Geomembranes, Vol. 52, Issue 1, 2024, pp. 95–109.
[18] Phutthananon C., Jongpradist P., Yensri P. and Jamsawang P., Dependence of ultimate bearing capacity and failure behavior of T-shaped deep cement mixing piles on enlarged cap shape and pile strength. Computers and Geotechnics, Vol. 97, 2018, pp. 27–41.
[19] Sukkarak R., Jongpradist P., Kongkitkul W., Jamsawang P. and Likitlersuang S., Investigation on load-carrying capacity of geogrid-encased deep cement mixing piles. Geosynthetics International, Vol. 28, Issue 5, 2021, pp. 450–463.
[20] Phutthananon C., Jongpradist P., Dias D., Guo X., Jamsawang P. and Baroth J., Reliability-based settlement analysis of embankments over soft soils reinforced with T-shaped deep cement mixing piles. Frontiers of Structural and Civil Engineering, Vol. 16, Issue 5, 2022, pp. 638–656.
[21] Phutthananon C., Jongpradist P., Kandavorawong K., Dias D., Guo X. and Jamsawang P., Reliability assessment for serviceability limit states of stiffened deep cement mixing column-supported embankments. Journal of Rock Mechanics and Geotechnical Engineering, Vol. 15, Issue 9, 2023, pp. 2402–2422.
[22] Imam R., Zarei M. and Ghafarian D., Relative contribution of various deformation mechanisms in the settlement of floating stone column-supported foundations. Computers and Geotechnics, Vol. 134, 2021, pp. 104109.
[23] Naue GmbH & Co. KG. Specifications of secugrid®. naue.com. August 2020, Retrieved June 1, 2024, from https://www.naue.com/info-center/downloads/specifications.
[24] Ghazavi M. and Afshar J., Bearing capacity of geosynthetic encased stone columns. Geotextiles and Geomembranes, Vol. 38, 2013, pp. 26–36.
[25] Ambily A.P. and Gandhi S.R., Behavior of stone columns based on experimental and FEM analysis. Journal of Geotechnical and Geoenvironmental Engineering, Vol. 133, Issue 4, 2007, pp. 405–415.
[26] Chen J.F., Han J., Oztoprak S. and Yang X.M., Behavior of single rammed aggregate piers considering installation effects. Computers and Geotechnics, Vol. 36, Issue 7, 2009, pp. 1191–1199.
[27] Killeen M.M. and Mccabe B.A., Settlement performance of pad footings on soft clay supported by stone columns: a numerical study. Soils and Foundations, Vol. 54, Issue 4, 2014, pp. 760–776.
[28] Khabbazian M., Kaliakin V.N. and Meehan C.L., Column supported embankments with geosynthetic encased columns: validity of the unit cell concept. Geotechnical and Geological Engineering, Vol. 33, Issue 3, 2015, pp. 425–442.
[29] Stark T.D. and Yacyshyn B.M., Specifications for constructing and load testing stone columns in clays. ASTM Special Technical Publication, Issue 1089, 1991, pp. 73–84.
[30] Yoo C., Performance of geosynthetic-encased stone columns in embankment construction: numerical investigation. Journal of Geotechnical and Geoenvironmental Engineering, Vol. 136, Issue 8, 2010, pp. 1148–1160.